SPECIAL
Connecting the Tropics to the Polar Regions
COLLECTION

A Multidecadal-Scale Tropically Driven Global Teleconnection over the Past Millennium and Its Recent Strengthening

XIAOFANG FENG,[a,b] QINGHUA DING,[b] LIGUANG WU,[c] CHARLES JONES,[b] IAN BAXTER,[b] ROBERT TARDIF,[d]
SAMANTHA STEVENSON,[e] JULIEN EMILE-GEAY,[f] JONATHAN MITCHELL,[g,h] LEILA M. V. CARVALHO,[b]
HUIJUN WANG,[a,i] AND ERIC J. STEIG[j]

[a] *Key Laboratory of Meteorological Disaster, Ministry of Education, Nanjing University of Information Science and Technology, Nanjing, China*
[b] *Department of Geography, and Earth Research Institute, University of California, Santa Barbara, Santa Barbara, California*
[c] *Department of Atmospheric and Oceanic Sciences and Institute of Atmospheric Sciences, Fudan University, Shanghai, China*
[d] *Department of Atmospheric Sciences, University of Washington, Seattle, Washington*
[e] *Bren School of Environmental Science and Management, University of California, Santa Barbara, Santa Barbara, California*
[f] *Department of Earth Sciences, University of Southern California, Los Angeles, California*
[g] *Department of Atmospheric and Oceanic Sciences, University of California, Los Angeles, Los Angeles, California*
[h] *Department of Earth, Planetary and Space Sciences, University of California, Los Angeles, Los Angeles, California*
[i] *Collaborative Innovation Center on Forecast and Evaluation of Meteorological Disasters, Nanjing University of Information Science and Technology, Nanjing, China*
[j] *Department of Earth and Space Sciences, University of Washington, Seattle, Washington*

(Manuscript received 25 March 2020, in final form 1 December 2020)

ABSTRACT: In the past 40 years, the global annual mean surface temperature has experienced a nonuniform warming, differing from the spatially uniform warming simulated by the forced responses of large multimodel ensembles to anthropogenic forcing. Rather, it exhibits significant asymmetry between the Arctic and Antarctic, with intermittent and spatially varying warming trends along the Northern Hemisphere (NH) midlatitudes and a slight cooling in the tropical eastern Pacific. In particular, this ‘‘wavy’’ pattern of temperature changes over the NH midlatitudes features strong cooling over Eurasia in boreal winter. Here, we show that these nonuniform features of surface temperature changes are likely tied together by tropical eastern Pacific sea surface temperatures (SSTs), via a global atmospheric teleconnection. Using six reanalyses, we find that this teleconnection can be consistently obtained as a leading circulation mode in the past century. This tropically driven teleconnection is associated with a Pacific SST pattern resembling the interdecadal Pacific oscillation (IPO), and hereafter referred to as the IPO-related bipolar teleconnection (IPO-BT). Further, two paleo-reanalysis reconstruction datasets show that the IPO-BT is a robust recurrent mode over the past 400 and 2000 years. The IPO-BT mode may thus serve as an important internal mode that regulates high-latitude climate variability on multidecadal time scales, favoring a warming (cooling) episode in the Arctic accompanied by cooling (warming) over Eurasia and the Southern Ocean (SO). Thus, the spatial nonuniformity of recent surface temperature trends may be partially explained by the enhanced appearance of the IPO-BT mode by a transition of the IPO toward a cooling phase in the eastern Pacific in the past decades.

KEYWORDS: Antarctica; Arctic; Tropics; Teleconnections; Paleoclimate; Multidecadal variability

1. Introduction

Global surface temperatures have been warming significantly in the past 40 years due to anthropogenic forcing associated with increases in greenhouse gases (e.g., Lacis et al. 2010). However, the warming over this time has exhibited a prominent asymmetry (Maksym et al. 2012; Ji et al. 2014), characterized by strong warming in and around the Arctic with pronounced sea-ice and land-ice melting (Serreze and Barry 2011; Vaughan et al. 2013), but slight cooling over the Southern Ocean (SO) and no long-term change in total sea ice extent surrounding the Antarctic (Marshall et al. 2014, 2015; Armour et al. 2016). Understanding the causes of this asymmetry has attracted substantial scientific interest because, from energy balance considerations, CO_2 forcing alone should presumably induce uniform warming everywhere on the globe in a first-order approximation (Hansen et al. 2010). Thus, this bipolar contrast has been attributed to a combined effect of CO_2 forcing along with a number of additional factors, including CO_2-induced Arctic amplification (Serreze et al. 2009; Screen and Simmonds 2010), ocean heat transport driven by climatological oceanic circulation (Marshall et al. 2014, 2015; Armour et al. 2016), a cooling effect over the Antarctic caused by stratospheric ozone depletion (Goosse et al. 2009), and internal climate variability over different regions (Ding et al. 2011, 2014; Trenberth et al. 2014; Deser et al. 2017). Another striking feature of surface temperature changes in the past

---

Corresponding author: Qinghua Ding, qinghua@ucsb.edu

DOI: 10.1175/JCLI-D-20-0216.1

decades is a strong wave train–like structure of temperature trends in the Northern Hemisphere (NH) midlatitudes, which promotes a significant winter cooling over Eurasia in the past decades (e.g., Ding et al. 2011, 2014; Mori et al. 2014). This pattern, in turn, has been suggested to be driven by significant sea ice melting in the Arctic. The wintertime cooling over Eurasia along with its suggested driving force from the north is commonly referred to as the warm Arctic–cold Eurasia (WACE) pattern (Cohen et al. 2012; Mori et al. 2014). However, there are diverse opinions and a lack of consensus about the ultimate driver of the WACE and how the WACE interacts with Arctic warming, extratropical circulation, and tropical forcing (Mori et al. 2014; Overland et al. 2015; Sun et al. 2016). Although many theories have been proposed to explain individual regional climate anomalies in the past decades, an integrated and comprehensive understanding of all these key features and their behaviors in a global context over longer periods remains elusive.

It is also noteworthy that climate models subject to CO_2 forcing and ozone depletion cannot fully replicate these observed temperature trends in the Arctic, the Antarctic, and the NH midlatitudes (Ding et al. 2014). The degree to which this is due to a failure of model simulations to capture important processes, as opposed to being affected by low-frequency natural variability over these areas in the past decades, remains uncertain. Recent studies have noted that global atmospheric circulation driven by low-frequency tropical sea surface temperature (SST) variability may be essential to explain changes in the Arctic, Antarctic, and midlatitudes in the past century (Schneider and Steig 2008; Trenberth et al. 2014; Deser et al. 2017; Meehl et al. 2018). However, how tropical SST regulates extratropical climate on multidecadal time scales over an expanded time period beyond the past century is unknown since understanding this linkage is hampered by the brevity of the instrumental record and twentieth-century reanalyses. Two recently available paleo-reanalysis reconstruction datasets, the ensemble Kalman fitting 400-yr paleo-reanalysis (EKF400) (Franke et al. 2017) and the Last Millennium Reanalysis version 2.0 (LMR2) (Tardif et al. 2019), contain reconstructions of atmospheric circulation over the past four centuries and two millennia, respectively. They thus provide the first opportunity to achieve this goal and further build understanding of whether the leading teleconnection pattern in the recent decades reflects a recurrent internal mode over the past 400 and 2000 years. This approach will place recent global circulation changes into a long-term context to lend more confidence in assessing the importance of internal variability to the recent global climate trends.

2. Data and methods

a. Reanalyses, EKF400, LMR2, and CCSM4

We use monthly geopotential height and surface temperature from six reanalysis datasets, including ERA-Interim (Dee et al. 2011) from 1979 to 2017, ERA-40 (Uppala et al. 2005) from 1958 to 2001, ERA-20C (Stickler et al. 2014) from 1900 to 2010, the Japanese 55-year Reanalysis (JRA-55) (Kobayashi et al. 2015) from 1958 to 2017, National Centers for Environmental Prediction Reanalysis data (NCEP) (Kalnay et al. 1996) from 1948 to 2017, and the National Oceanic and Atmospheric Administration (NOAA) Twentieth Century Reanalysis (20CR) (Compo et al. 2011) from 1900 to 2014. The monthly global SST in 1900–2017 is taken from the NOAA extended reconstructed SST version5 (ERSSTv5) (Huang et al. 2017). We additionally use a 400-yr paleo-reanalysis reconstruction dataset, which utilizes an ensemble Kalman fitting method to assimilate multiple observations (including instrumental observations, historical climate indices, and proxy data) with ECHAM5.4 AGCM simulations (EKF400; Franke et al. 2017). This dataset provides monthly geopotential height at 500 hPa and surface temperatures over the period from 1603 to 2003, which allows us to better examine global circulation variability in each season over the past 400 years. We also use a set of the last two millennia reconstruction reanalysis, the Last Millennium Reanalysis version 2.0 (LMR2) (Tardif et al. 2019), combining the Community Climate System Model version 4.0 (CCSM4) (Landrum et al. 2013) and proxy data from the PAGES 2k version 2 (PAGES2k Consortium 2017) and other data collections (Anderson et al. 2019). The last millennium simulation CCSM4, a coupled atmosphere–ocean–sea ice simulation covering the period from 850 to 1850, is used as the base model in LMR2. The CCSM4 simulations use the Community Atmosphere Model version 4 (CAM4) and external forcing that includes volcanic eruptions, total solar irradiance, and the principal long-lived greenhouse gases (e.g., CO_2, CH_4, and N_2O). More details on the CCSM4 and how it is combined with proxies in generating the reconstruction reanalysis LMR2 can be found in Landrum et al. (2013) and Tardif et al. (2019). The 500-hPa geopotential height and surface temperatures in LMR2 used in this study are an ensemble mean of 20 Monte Carlo realizations each using a 100-member ensemble (grand total of 2000 members) and are only available at annual mean resolution. In addition, we repeat the same analyses conducted in this study on the newly available LMR2.1 and find a very similar teleconnection pattern as that derived from LMR2, so our discussion focuses on results from LMR2.

b. CMIP5 and five model large ensembles

To examine the effects of increasing anthropogenic forcing on global climate, we use two sets of multimodel ensemble means to reduce uncertainties in each model (Deser et al. 2020). One is the ensemble mean of all 40 climate models provided in CMIP5 (Taylor et al. 2012; Table 1) over the 1979–2017 period, combining model outputs from the 1979–2005 historical runs and RCP8.5 forcing for 2006–17. The other is a five-model large ensemble (LE) mean from currently available fully coupled Earth system models, including the GFDL-CM3 20-member LE (GFDL-LE) (Griffies et al. 2011), the CSIRO-Mk3L 30-member LE (CSIRO-LE) (Phipps et al. 2011, 2012), the CESM1 40-member LE (CESM-LE) (Kay et al. 2015), the CanESM2 50-member LE (CanESM-LE) (Kirchmeier-Young et al. 2017), and the Max Planck Institute 100-member Grand Ensemble (MPI-GE) (Maher et al. 2019).

TABLE 1. List of the 40 global climate models in CMIP5.

No.	Model	Research center
1	BCC_CSM1.1	Beijing Climate Center, China Meteorological Administration, China
2	BCC_CSM1.1(m)	Beijing Climate Center, China Meteorological Administration, China
3	BNU-ESM	College of Global Change and Earth System Science, Beijing Normal University, China
4	CanESM2	Canadian Centre for Climate Modeling and Analysis, Canada
5	CCSM4	National Center of Atmospheric Research, United States
6	CESM1-BGC	Community Earth System Model Contributors, United States
7	CESM1-CAM5	Community Earth System Model Contributors, United States
8	CESM1-FASTCHEM	Community Earth System Model Contributors, United States
9	CESM1-WACCM	Community Earth System Model Contributors, United States
10	CMCC-CESM	Centro Euro-Mediterraneo per I Cambiamenti Climatici, Italy
11	CMCC-CM	Centro Euro-Mediterraneo per I Cambiamenti Climatici, Italy
12	CMCC-CMS	Centro Euro-Mediterraneo per I Cambiamenti Climatici, Italy
13	CNRM-CM5	National Center of Meteorological Research, France
14	CNRM-CM5.2	National Center of Meteorological Research, France
15	CSIRO Mk3.6.0	Commonwealth Scientific and Industrial Research Organization/Queensland Climate Change Center of Excellence, Australia
16	EC-EARTH	EC-EARTH consortium, Europe
17	FGOALS-g2	LASG, Institute of Atmospheric Physics, Chinese Academy of Sciences, China
18	FIO-ESM	The First Institute of Oceanography, SOA, China
19	GFDL CM3	NOAA Geophysical Fluid Dynamics Laboratory, United States
20	GFDL-ESM2G	NOAA Geophysical Fluid Dynamics Laboratory, United States
21	GFDL-ESM2M	NOAA Geophysical Fluid Dynamics Laboratory, United States
22	GISS-E2-H	NASA Goddard Institute for Space Studies, United States
23	GISS-E2-H-CC	NASA Goddard Institute for Space Studies, United States
24	GISS-E2-R	NASA Goddard Institute for Space Studies, United States
25	GISS-E2-R-CC	NASA Goddard Institute for Space Studies, United States
26	HadCM3	Met Office Hadley Center, United Kingdom
27	HadGEM2-AO	Met Office Hadley Center, United Kingdom
28	HadGEM2-CC	Met Office Hadley Center, United Kingdom
29	HadGEM2-ES	Met Office Hadley Center, United Kingdom
30	INM-CM4	Institute for Numerical Mathematics, Russia
31	IPSL-CM5A-LR	Institut Pierre Simon Laplace, France
32	IPSL-CM5A-MR	Institut Pierre Simon Laplace, France
33	IPSL-CM5B-LR	Institut Pierre Simon Laplace, France
34	MIROC5	Atmosphere and Ocean Research Institute (The University of Tokyo), National Institute for Environmental Studies, and Japan Agency for Marine-Earth Science and Technology, Japan
35	MIROC-ESM	Japan Agency for Marine-Earth Science and Technology, Atmosphere and Ocean Research Institute (The University of Tokyo), and National Institute for Environmental Studies Japan
36	MIROC-ESM-CHEM	Japan Agency for Marine-Earth Science and Technology, Atmosphere and Ocean Research Institute (The University of Tokyo), and National Institute for Environmental Studies Japan
37	MPI-ESM-LR	Max Planck Institute for Meteorology, Germany
38	MPI-ESM-MR	Max Planck Institute for Meteorology, Germany
39	MRI-CGCM3	Meteorological Research Institute, Japan
40	NorESM1-M	Norwegian Climate Center, Norway

c. Examination of proxy data performance in LMR2

LMR2 assimilates more than 2000 proxy records from the PAGES 2k version 2 (PAGES2k Consortium 2017) and the additional proxy records (Anderson et al. 2019). In the following analysis, we evaluate to what extent the temperature output from LMR2 reflects these records. We therefore select the 550 records from PAGES 2k version 2 considered in LMR2 since these were more carefully screened for temperature sensitivity. We also consider only proxies that have correlation coefficients with LMR2 surface temperatures higher than 0.2 and have effective record lengths longer than 100 years. Based on these criteria, we select 265 records that best reflect temperature variability. It should be noted that the availability of proxy data over the NH assimilated into LMR2 is much denser than in the Southern Hemisphere (SH), which may lead to larger uncertainties of LMR2 data in the SH. For example, only 5.8% (32 records) of the 550 records from PAGES 2k version 2 were obtained south of 30°S and used in LMR2.

d. Methods to minimize the effects of external forcing

To reduce the influence of external radiative forcing on reanalysis data over the past 40 years, we use a linear detrending method. However, since changes of greenhouse gases and aerosol concentrations over the twentieth century are not monotonic, the linear detrending method is not effective for minimizing the effects of external forcing over longer periods (Christidis and Stott 2015). Thus, we construct a global mean geopotential height index (area weighted) to measure the overall effect of external radiative forcing on the global mean height change and then linearly regress out this global mean variability from the geopotential height fields in each grid cell. We also examine a number of alternative ways to achieve this goal and find that the results are not sensitive to the approach to preprocess the datasets in our studies.

e. Significance of correlation

We consider the "effective sample size" N^* (Bretherton et al. 1999) to evaluate the statistical significance of the correlation coefficient throughout the paper. To calculate N^* of two time series, we account for the autocorrelation in the time series by using the following equation:

$$N^* = N\frac{1 - r_1 r_2}{1 + r_1 r_2},$$

where N is the number of available time steps and r_1 and r_2 are lag-one autocorrelation coefficients of each variable. A confidence level above 95% is used in this study to determine the significance of correlations and composites.

3. Observed and simulated temperature and circulation trends in the past 40 years

Annual mean 200- and 500-hPa geopotential height (Z200 and Z500) trends in the past 40 years show a hemispheric asymmetry in the high latitudes with the largest height rise in the NH and a slight decrease in the SH (Figs. 1a,d). This hemispheric asymmetry is likely due to a Rossby wave train emanating from the tropical eastern Pacific and propagating in both meridional directions toward high latitudes. We can better reveal the structure of this wave train by removing the zonal mean component from trends at each latitude over the period 1979–2013 during which the tropical eastern Pacific SST experienced a significant cooling (Figs. 2a,b). This global wave train consists of high pressure in the Arctic, low pressure in the Amundsen Sea, and a zonal wavenumber-3 structure in the NH midlatitudes. The source of the wave train from the Pacific to the two poles appears to be the tropical atmospheric response to the cooling SST trend in the eastern Pacific (Fig. 1g). Several early studies (Ding et al. 2014; Trenberth et al. 2014) have shown that different climate models forced by the observed SST cooling over the tropical eastern Pacific can generate a similar two-pronged large-scale Rossby wave train extending from the tropical Pacific to the Arctic and West Antarctic separately (Fig. 2c).

Surface temperature trends also correspond well with the large-scale circulation trends. In the NH midlatitudes, a chain of intermittent warming trends coincides with a zonal wavenumber-3 pattern in Z200 and Z500 (Fig. 1g). A key feature of this midlatitude pattern is the near-zero trend over central Asia where a strong cooling trend is observed in boreal winter (Cohen et al. 2012; Mori et al. 2014; Sun et al. 2016). In addition, the largest upper-level geopotential height rise, found in the Arctic, is associated with the greatest surface and atmospheric warming, as well as accelerating sea-ice and land-ice melting (Ding et al. 2014; Hahn et al. 2018). Weak surface cooling in the SH high latitudes coincides with negative geopotential height trends, further highlighting the asymmetric nature of surface temperature trends in the past 40 years. This correspondence suggests that the large-scale circulation pattern plays a key role in shaping the pattern of surface temperature trends through circulation-driven thermal and dynamical impacts (Holland and Kwok 2012; Ding et al. 2014).

In contrast to the observed trends, the CMIP5 and five model large ensemble mean linear trends under the increase of CO_2 forcing and ozone depletion over the same period (1979–2017) show uniform warming everywhere with slightly larger height rise in the tropics at upper levels (e.g., Z200; Figs. 1b,c), reflecting a temperature response to anthropogenic forcing expected under the constraint of the moist adiabatic lapse rate (Fu et al. 2011). In particular, the observed regional temperature and circulation changes in the Arctic, SO, and Eurasia are not present in the forced response and tropical SST shows a uniform warming without a cooling signal in the eastern Pacific (Figs. 1h,i). This discrepancy between the spatially uniform simulated trends opposed to heterogeneous observed trends is because model ensemble means primarily reflect our best estimate of the forced response to increasing anthropogenic forcing. Thus, the observed features likely reflect a combination of anthropogenic forcing and internal variability possibly originating from the tropics.

4. The leading internal mode of global circulation in the past 40 years

To explore whether the global wave train revealed in the trends of observed Z200 and Z500 represents an actual physical mode tying together regional circulation variability across

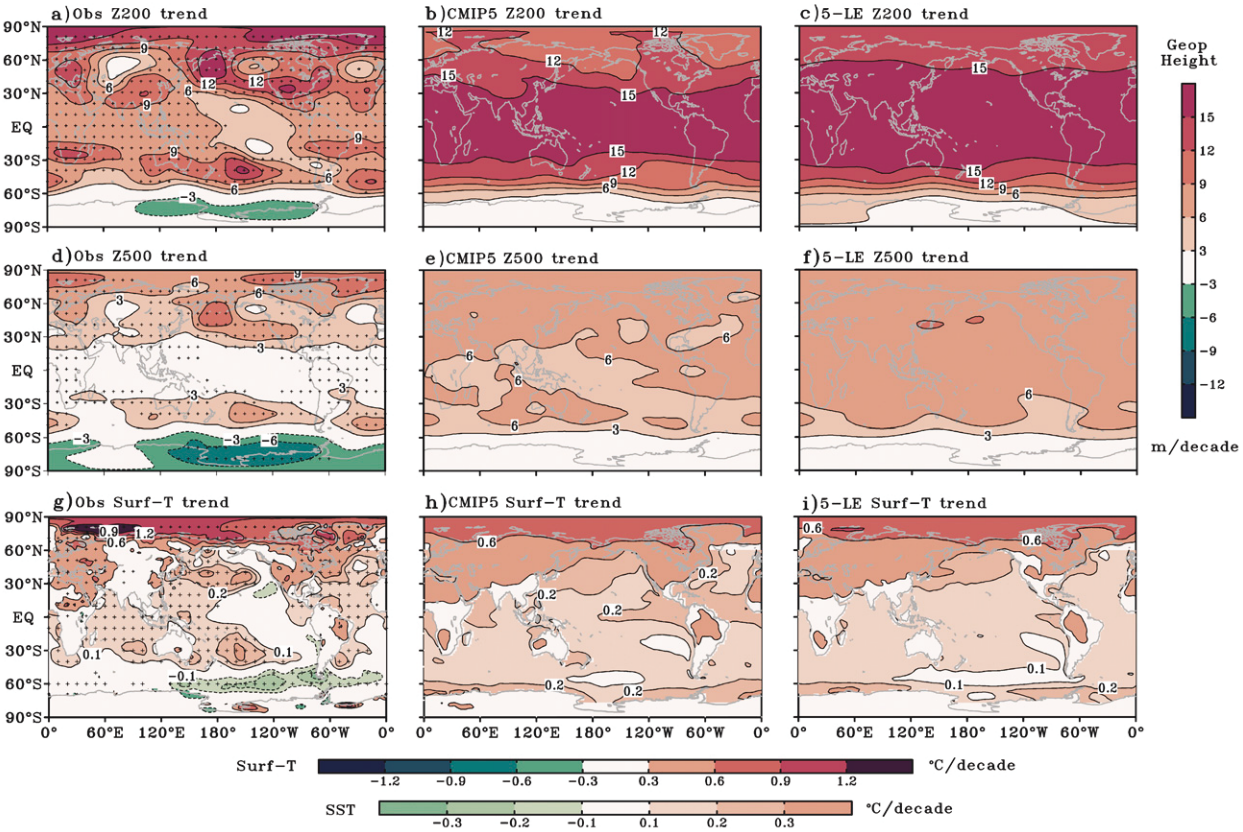

FIG. 1. Linear trends of annual mean 200-hPa geopotential height (Z200; m decade^{-1}) over the period from 1979 to 2017 in (a) ERA-Interim, (b) 40-member ensemble mean of CMIP5, and (c) the mean of five large ensemble (LE) historical simulations. (d)–(f),(g)–(i) As in (a)–(c), but for annual mean 500-hPa geopotential height (Z500; m decade^{-1}) and surface temperatures (°C decade^{-1}), respectively. In (g), different color scales are used for ERA-Interim surface temperature trends over the land in the globe and ERSSTv5 trends in oceans. Grid points with trends that are statistically significant at the 95% confidence level are denoted by small crosses in (a), (d), and (g). Linear trends of all grid points are statistically significant at the 95% confidence level in model responses in (b), (c), (e), (f), (h), and (i).

the globe, we employ empirical orthogonal function (EOF) analysis of global annual mean detrended geopotential height to examine whether leading EOFs share a similarity with the pattern of observed trends. After linear detrending, Z200 variability in the residual field retains nearly 90% of its total variance. The first EOF mode (EOF1) of residual Z200 shows a global teleconnection propagating from the tropics to the two poles with high pressure around the Arctic but low pressure around the SO in the positive phase, and a zonal wavenumber-3 structure in the NH midlatitudes (Fig. 3a). This leading internal mode bears a striking resemblance to the observed Z200 trends (Fig. 2b), indicating that these linear trends are also likely of internal origin and thus may share a similar underlying mechanism.

Correlations of surface temperatures with the principal component of EOF1 (PC1) show a warming Arctic over Greenland and northeastern Canada, cooling over the Pacific sector of the SO, and cooling SST in the tropical eastern Pacific, similar to the observed linear trends in Fig. 1g (Fig. 3c). It also coincides with a zonal wavenumber-3 pattern in the NH midlatitude Z200 with cooling anomalies over the continents in the NH. This cooling signal over Eurasia suggests that this internal mode may be partially responsible for the appearance of the WACE pattern through a Rossby wave propagation along the NH midlatitudes. Atmospheric wave activity shows clear energy transport from the tropics to the two poles and wave energy propagation along the midlatitudes of the NH, where circulation anomalies are generated to regulate surface temperature changes (Fig. 3a). The EOF1 of Z500 exhibits a similar spatial pattern, suggesting that this leading mode has a barotropic structure (Fig. 3b), typical of extratropical teleconnections driven by tropical forcing. Because of this, we hereafter focus on Z500 to make a better comparison with LMR2, which only provides Z500 as a non-surface reconstructed variable.

5. The leading internal mode in all reanalyses, EKF400, and LMR2

To further understand whether the same global teleconnection remains intact over longer periods, we first

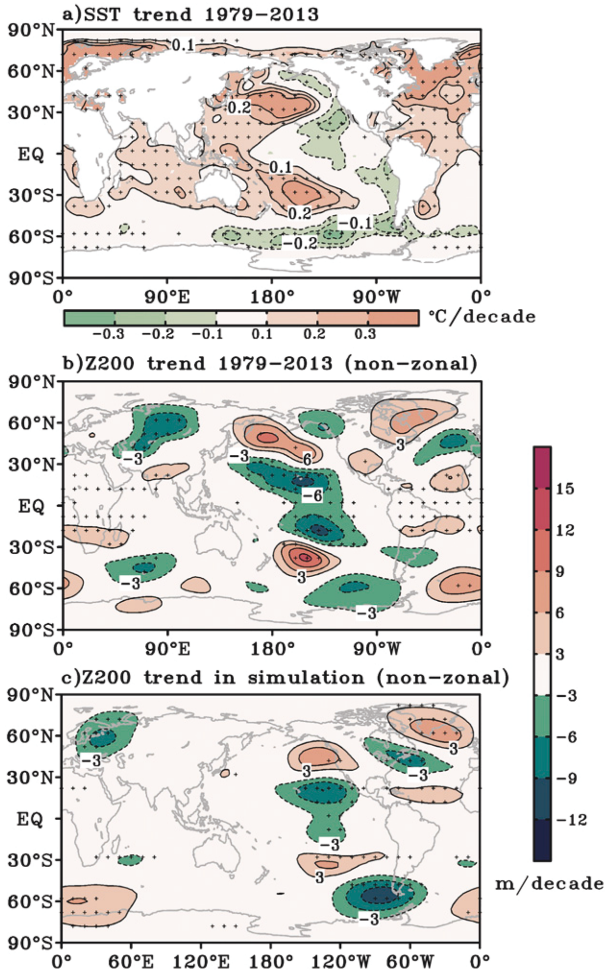

FIG. 2. Linear trends of (a) ERSSTv5 annual mean sea surface temperature (SST; °C decade^{-1}) and (b) the nonzonal component of ERA-Interim Z200 (m decade^{-1}) in 1979–2013. (c) Linear trends of the nonzonal component of annual mean Z200 in an Atmospheric Model Intercomparison Project (AMIP)-type ECHAM4 simulation (10-member ensemble mean) forced by the observed tropical SST between 30°S and 30°N in 1979–2013. In the extratropics, a slab ocean/sea ice model is utilized to consider local air–sea interactions. The model result is adopted from Ding et al. (2014) but extended to the SH. Grid points with trends that are statistically significant at the 95% confidence level are denoted by small crosses.

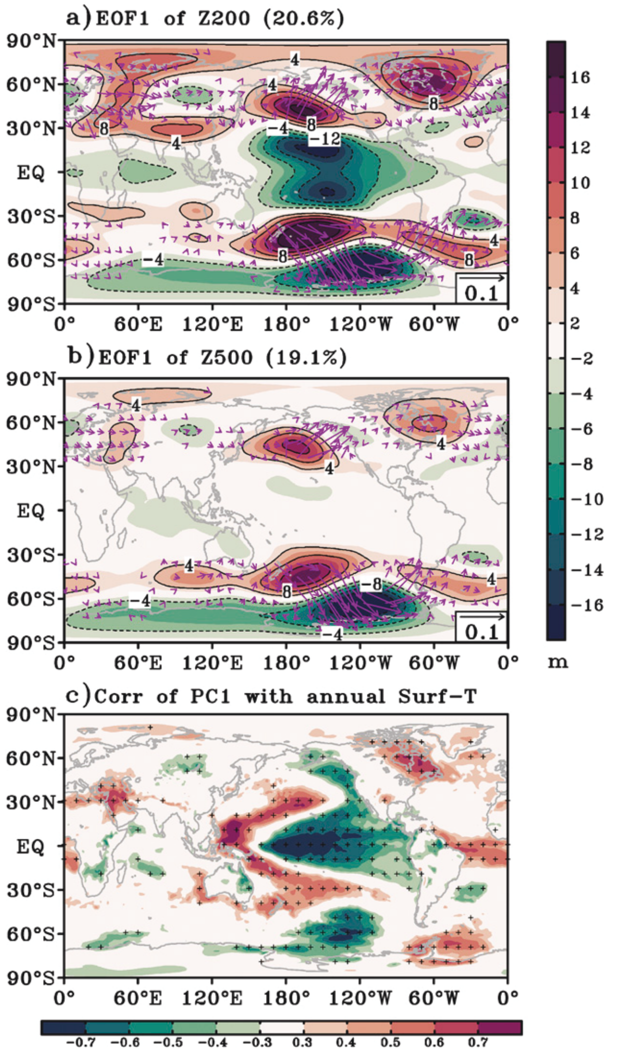

FIG. 3. EOF1 of annual mean residual (a) Z200 and (b) Z500 fields after linear detrending during the period of 1979–2017. (c) Correlations of Z200 PC1 with annual mean residual surface temperatures from 1979 to 2017. In (a) and (b), purple vectors (10^4 Pa m^2 s^{-2}; vectors less than 10^3 Pa m^2 s^{-2} are omitted) denote the wave activity flux (Plumb 1985) associated with the corresponding EOF pattern. The total variance explained by each EOF is indicated in the parentheses. In (c), stippling indicates statistically significant correlations at the 95% confidence level.

examine the leading EOFs of Z500 from five reanalyses over the twentieth century. We construct an index by averaging global mean Z500 (area weighted; Fig. 4) to measure the overall effect of external radiative forcing, and then regress out this global mean variability from the Z500 fields in each grid. After reducing effects of external forcing for all reanalyses over the twentieth century, the residual Z500 fields still retain 82%–90% of their total variance. The teleconnection mode can be captured in all these reanalyses as the second EOF (EOF2; Figs. 5a–e). To reduce uncertainties associated with different model setup and assimilation schemes in reanalysis datasets, and link this mode with surface temperatures, we use the average of PCs across all six reanalyses over the past century (PC1 in the past 40 years and PC2s in the five reanalyses) to create an ensemble-PC index (Fig. 5g). Correlations of the index with surface temperatures are associated with hemispheric asymmetry in the high latitudes and cold tropical SST in the eastern Pacific throughout the last hundred years (Figs. 5h–j). These patterns share some similarities with the interdecadal Pacific oscillation (IPO), and the IPO index

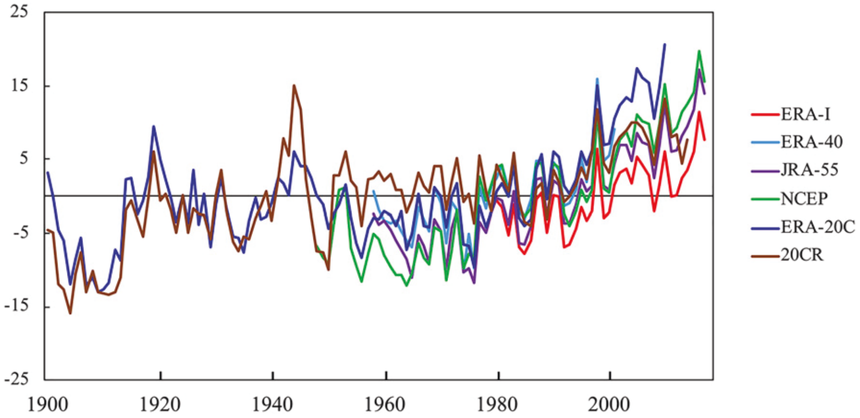

FIG. 4. Time series of normalized global mean Z500 (m) from six reanalyses (ERA-Interim in 1979–2017, ERA-40 in 1958–2001, JRA-55 in 1958–2017, NCEP in 1948–2017, ERA-20C in 1900–2010, and 20CR in 1900–2014).

(Henley et al. 2015) is strongly correlated with the ensemble-PC index in the period of 1900–2017 ($r = -0.85$). This suggests that this bipolar teleconnection mode is closely associated with SST variability in the tropical eastern Pacific. Thus, it is hereafter referred to as the IPO-related bipolar teleconnection (IPO-BT) and the related index is referred to as the IPO-BT index.

To detect whether the IPO-BT exists over the past 400 years, we employ EOF analysis on annual mean Z500 in EKF400 after reducing the effects of external forcing by regressing out the global mean Z500. The IPO-BT mode can be captured as EOF1 in EKF400 (Fig. 6a), similar to that in all reanalyses (Figs. 3b and 5a–e), especially in the NH. Over their overlapping period from 1900 to 2003, PC1 of residual Z500 in EKF400 (PC1-EKF400; Fig. 6b) is significantly correlated with the IPO-BT index ($r = 0.41$). The correlation of PC1-EKF400 over the past 400 years is calculated with annual mean surface temperature in EKF400 (Fig. 6c) and the pattern bears a strong resemblance to the IPO-BT-related temperature pattern in the past 40 and 100 years (Figs. 3c and 5h–j), exhibiting strong Arctic warming over Greenland and northeastern Canada, and cooling over Eurasia and the tropical Pacific. In particular, the linkage of the IPO-BT mode with the Eurasian cooling is most prominent in boreal winter (DJF; Fig. 6d), which additionally supports that the so-called WACE pattern, consisting of Eurasian cooling and Arctic warming, is partially associated with the IPO-BT and most significant in winter over the past 400 years.

To further examine the IPO-BT's variability over the past two millennia, it is desired to repeat our EOF analysis on global Z500 field in LMR2. However, it is unclear whether LMR2 data in the SH have the same quality as those in the NH considering that fewer proxy data from the SH are used in LMR2. During the recent 100-yr period (1900–2000), PC2 of residual Z500 in LMR2 resembles the IPO-BT index ($r = 0.42$), and the corresponding EOF2 shows pattern similar to the IPO-BT in the NH, but not in the SH (Fig. 5f). We also find that atmospheric circulation variability is better captured in the NH than the SH by comparing time series of normalized Z500 averaged in the tropics and the high latitudes in the two hemispheres, separately, from LMR2 and all reanalyses. The Z500 variability in the SH high latitudes has considerably less agreement between datasets than that in the NH and the tropics (Fig. 7). To quantify this difference, we calculate correlations of Z500 averaged in the tropics and in the high latitudes in the NH and the SH between any pair of all reanalyses during their overlapping periods (Fig. 8). There is high consistency of Z500 variability for most of the pairs in the tropics and the NH high latitudes. But for the SH, consistency is relatively weak, likely resulting from the limited availability of observations in the SH. Specifically, EOF1 in each of the five reanalyses over the twentieth century primarily captures a mode confined to the SH (Figs. 9a–e), which is likely affected by larger variability and uncertainties in the SH than the NH in the early periods. Another possible reason for the IPO-BT mode being captured as EOF1 rather than EOF2 in ERA-Interim in the past 40 years seems to be related to the strengthening of this internal mode by a transition of the IPO toward a cooling phase in the eastern Pacific in recent decades. Therefore, we should be cautious when examining climate variability in the SH over long periods considering that temporal and spatial inhomogeneity issues are common for current long-term reanalysis datasets.

Using NH-only data in LMR2 in the past 2000 years, we find that the second EOF mode (EOF2-LMR2) closely resembles the IPO-BT derived from ERA-Interim in the recent 40 years (spatial correlation coefficient = 0.47 in the NH) and in the past century. The pattern exhibits a tropically forced Rossby wave train and a zonal wavenumber-3 structure along the NH midlatitudes, with a significant height rise in the Arctic and a negative center over northern Eurasia and western North America (Fig. 10a). PC2 from LMR2 (PC2-LMR2) is also significantly correlated with PC1-EKF400 in the overlapping period of 1603–2000 ($r = 0.37$).

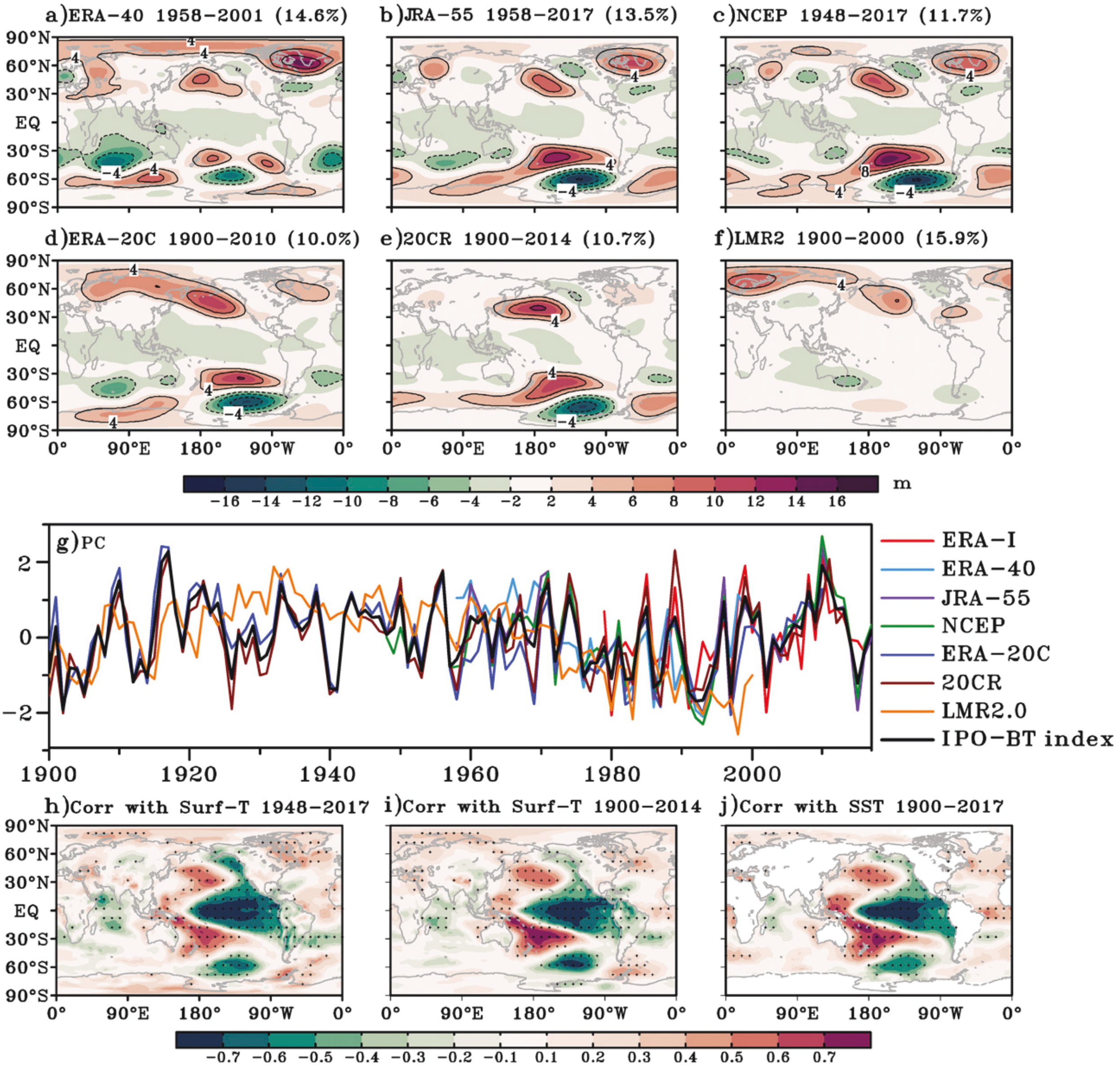

FIG. 5. EOF2 of annual mean residual Z500 in (a) ERA-40 in 1958–2001, (b) JRA-55 in 1958–2017, (c) NCEP in 1948–2017, (d) ERA-20C in 1900–2010, (e) 20CR in 1900–2014, and (f) LMR2 in 1900–2000. (g) The PC2 in the six reanalyses shown for (a)–(f) and PC1 in ERA-Interim. Correlations of the IPO-BT index [black lines in (g)] with annual mean residual surface temperatures in (h) NCEP in 1948–2017 and (i) 20CR in 1900–2014, and (j) residual SST in ERSSTv5 in 1900–2017. In (a)–(f), the total variance explained by each EOF is indicated in the parentheses. In (h)–(j), stippling indicates statistically significant correlations at the 95% confidence level.

Additionally, there is little sensitivity of our EOF analysis to differing periods from LMR2 spanning the last 1500, 1000, 500, and 200 years all ending in the year 2000, and the 1850 years before the industrial revolution. Correlations of PC2-LMR2 with LMR2 surface temperatures show that, like in the other reanalysis datasets, this mode coincides with a warm Arctic, cold Eurasia, and cold SST in the tropical eastern Pacific in the positive phase, further reinforcing that temperature changes in these three key regions are strongly linked by the IPO-BT (Fig. 10b). We also note that Arctic warming associated with the IPO-BT occurs mostly over Greenland in the past millennium, while the largest Arctic warming in the past 40 years mainly occurs in the Barents–Kara Seas (Fig. 1g), which is suggested to be related to an oceanic process referred to as ‘‘Atlantification’’ (Polyakov et al. 2017, 2020). The consistent warming over Greenland in all reanalyses, EKF400, and LMR2 suggests that the IPO-BT primarily contributes to

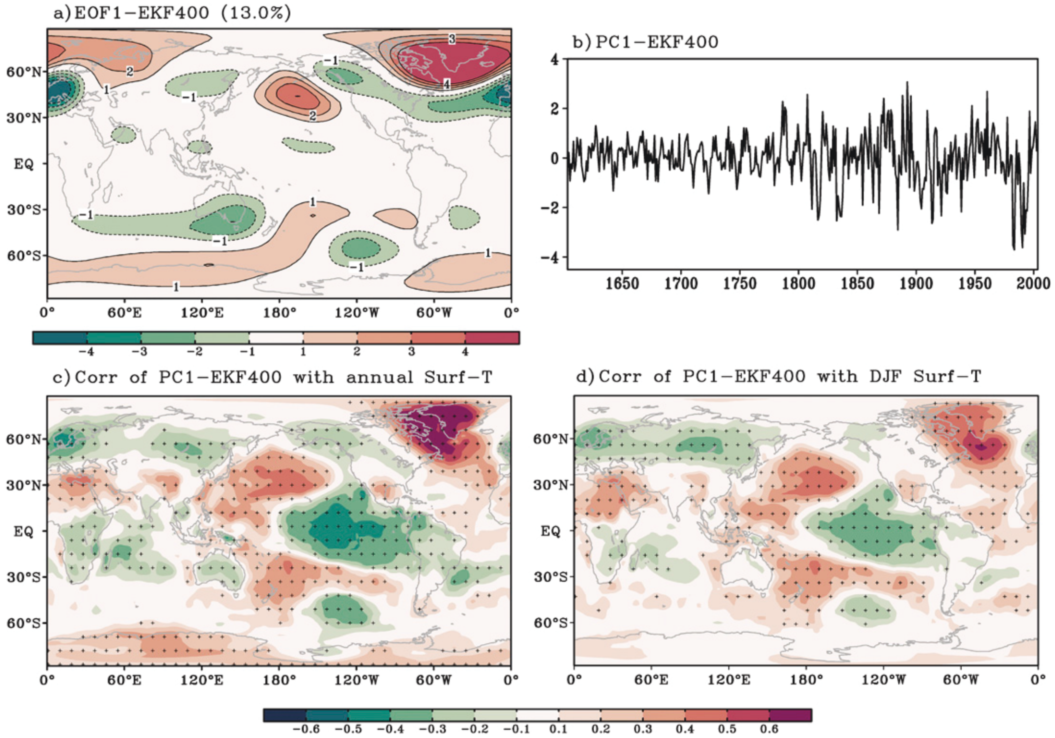

FIG. 6. (a) EOF1 of annual mean residual Z500 in EKF400 and (b) PC1-EKF400 during the period of 1603–2003. Correlations of PC1-EKF400 with (c) annual mean and (d) winter (DJF; i.e., December of the previous year and January and February of the current year) residual surface temperatures in EKF400. In (c) and (d), stippling indicates statistically significant correlations at the 99.9% confidence level with the effect sample size at 240.

the Arctic warming over Greenland and northeastern Canada and its role in causing the warming over the Barents–Kara Seas is unclear. PC2-LMR2 is also significantly correlated ($r = -0.2$) with a reconstructed IPO index (Buckley et al. 2019) from 1350 to 2000, suggesting there is sensitivity of the IPO-BT to the IPO over the past 650 years. While LMR2 has large uncertainty in the SH (fewer proxy records in the SH), correlations of PC2-LMR2 with global Z500 and surface temperature still show a IPO-BT-related cooling over the SO as was observed in the past 40 years, indicating that the IPO-BT-related bipolar contrast may have been present over the past two millennia. However, due to the limited records of proxy data in the SH, the southern branch of this bipolar mode cannot be clearly captured in the EOF analysis using the LMR2 global field.

In addition, the recent uptick in the global mean Z500 may potentially cause some artificial signals in the residual Z500 field after the regression in the past 2000 years. Thus, we apply EOF analysis on the NH annual mean residual Z500 during the periods before year 1850 or 1500 in LMR2, respectively, to examine whether the IPO-BT mode remains intact during the preindustrial periods. The IPO-BT mode can be captured as EOF2, which resembles EOF2-LMR2 derived from the entire period. The consistent results further suggest that the IPO-BT mode is a robust internal mode and it is not sensitive to how we remove external forcing before the EOF analysis.

6. Fingerprints of the IPO-BT in proxy data and CCSM4 simulations

LMR2 effectively captures the IPO-BT. However, the relative contributions of proxy data and CCSM4's physics in replicating the IPO-BT in LMR2 remains unclear. Thus, we evaluate how the IPO-BT is reflected in temperature variability from proxies by calculating correlations between individual proxy records and PC2-LMR2. Based on 265 proxies that are effectively reflected in LMR2 (see section 2c), correlations of PC2-LMR2 with these proxies and surface temperatures in LMR2 exhibit a high coherence; this consistency suggests that temperature variability over the Arctic and Eurasia is linked with the tropical eastern Pacific through the IPO-BT in the past two millennia (Fig. 10b). The dipole over the Arctic and Eurasia in LMR2 is similar to the observed WACE pattern in the recent 40 years (Fig. 10c). This signal reflected in proxies suggests that the WACE pattern could be partially synchronized by tropical SST variability through the IPO-BT over longer time periods.

We further investigate whether the out-of-phase relationship between the Arctic and tropics, connected via the

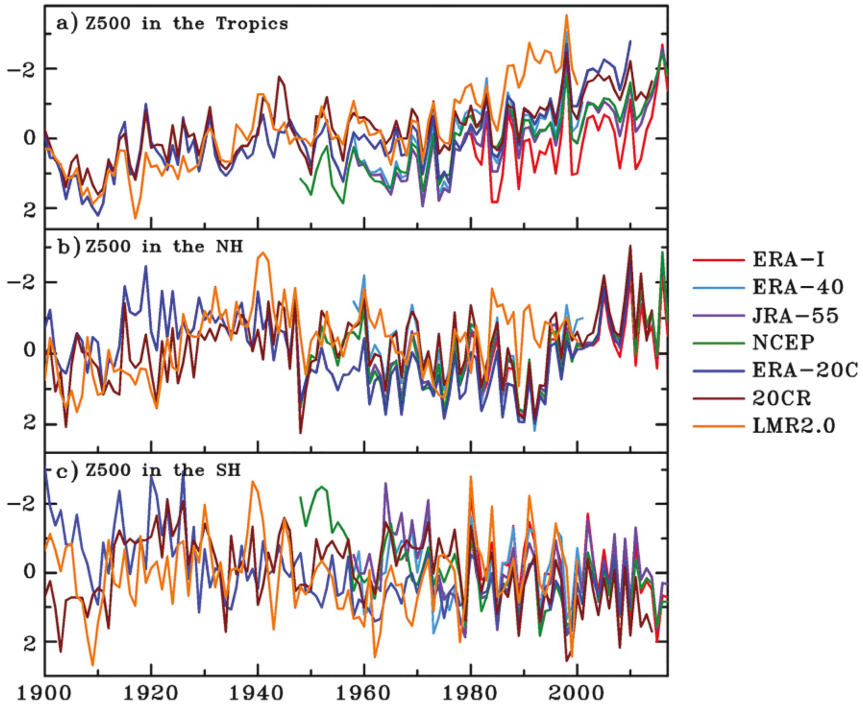

FIG. 7. Time series of normalized Z500 averaged in (a) the tropics (30°N–30°S) and the high latitudes in (b) the Northern Hemisphere (NH; 60°–90°N) and (c) the Southern Hemisphere (SH; 60°–90°S) from six reanalyses and LMR2.

IPO-BT, exists in the individual proxy records. The longest tropical record with data prior to the twentieth century is the Palmyra coral record (5.9°N, 197.9°E) (Cobb et al. 2013) in the eastern Pacific, spanning the time period from 928 to 1998 with several interspersed missing periods (a total of 532 available years). We use this longest coral record to correlate with all available proxy records in the Arctic and midlatitudes (15 records north of 70°N; Table 2; 133 records between 40° and 70°N) over the overlapping period of each pair. Most ice core records near Greenland, half of the Arctic records, show negative correlations, which would be expected under the influence of the IPO-BT (Fig. 10d). Among them, the Agassiz ice core record (80.7°N, 286.9°E) (Vinther et al. 2008) has the strongest negative correlation ($r = -0.23$) with the Palmyra coral record in the past millennium. Although some ice core records over the Kara Sea regions show weak positive correlations with the Palmyra coral record, the clustering of negative correlations in and around Greenland suggests that an out-of-phase linkage favored by the IPO-BT is most significant between temperature variability over Greenland and the tropical eastern Pacific. Proxy records over central Asia and along the west coast of North America also exhibit significant positive correlations with the Palmyra coral record. These relationships are the essential features of temperature variability associated

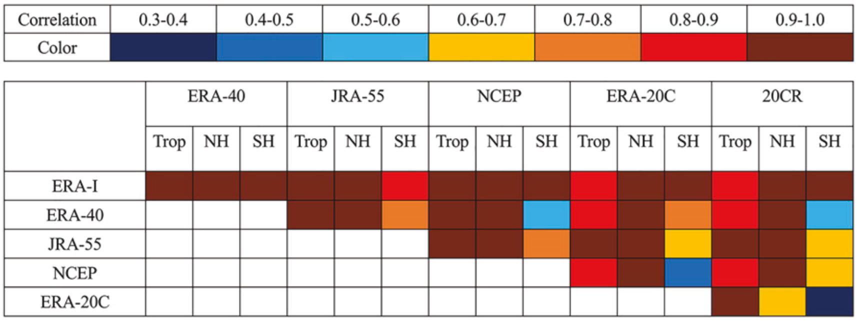

Correlation	0.3-0.4	0.4-0.5	0.5-0.6	0.6-0.7	0.7-0.8	0.8-0.9	0.9-1.0
Color	⬛	🟦	🔷	🟨	🟧	🟥	🟫

	ERA-40			JRA-55			NCEP			ERA-20C			20CR		
	Trop	NH	SH	Trop	NH	SH	Trop	NH	SH	Trop	NH	SH	Trop	NH	SH
ERA-I	🟫	🟫	🟫	🟫	🟫	🟥	🟫	🟫	🟫	🟥	🟫	🟫	🟥	🟫	🟫
ERA-40				🟫	🟫	🟧	🟫	🟫	🔷	🟥	🟫	🟧	🟥	🟫	🔷
JRA-55							🟫	🟫	🟧	🟫	🟫	🟨	🟫	🟫	🟨
NCEP										🟥	🟫	🟦	🟥	🟫	🟨
ERA-20C													🟫	🟨	⬛

FIG. 8. Correlations of Z500 averaged in the tropics (30°N–30°S) and the high latitudes in the NH (60°–90°N) and the SH (60°–90°S) between any pair out of the reanalysis datasets during their overlapping periods.

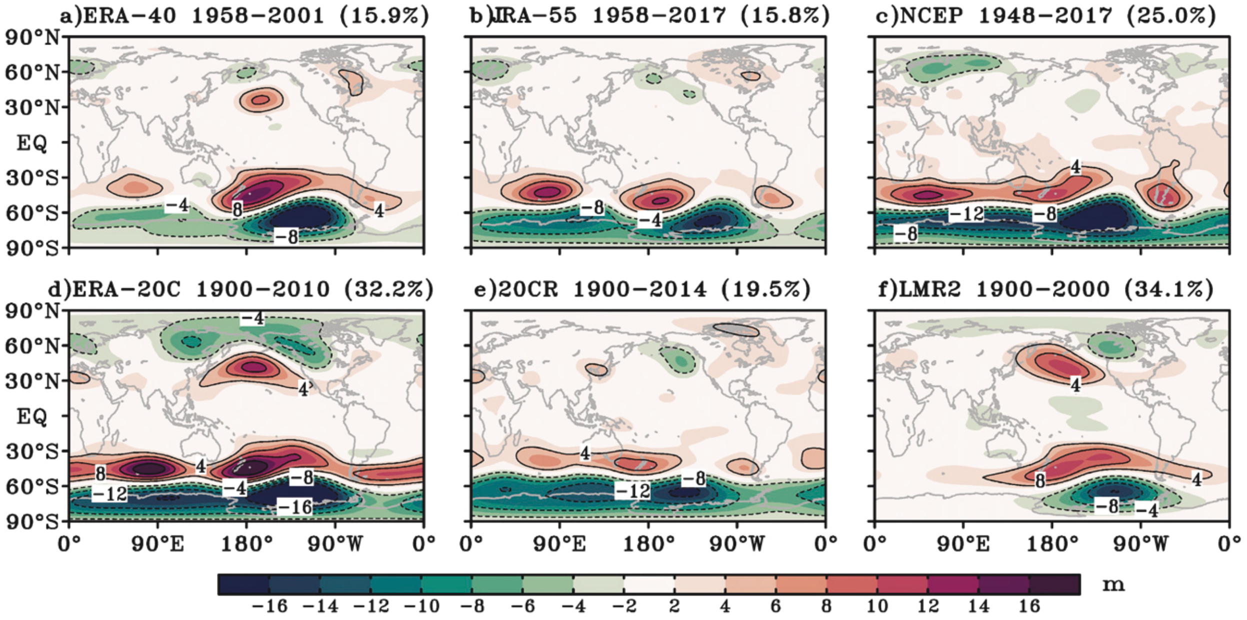

FIG. 9. As in Figs. 5a–f, but for EOF1 of each reanalysis and LMR2. The total variance explained by each EOF is indicated in the parentheses.

with the IPO-BT in the past 40 years. The consistency of the Arctic–tropical and midlatitude–tropical linkages reflected in these raw proxy data reinforces the existence of the IPO-BT in the past millennium.

On the other hand, inherent variability of the CCSM4, being the base model of LMR2, could also contribute to the appearance of an IPO-BT-like pattern in LMR2. Thus, we perform EOF analysis using Z500 in CCSM4 to obtain the IPO-BT for the nonproxy assimilative configuration of the model. Using a 1000-yr simulation of CCSM4, the external forcing is reduced in Z500 fields by linearly regressing out the area-weighted global mean geopotential height, which is representative of the overall externally forced radiative effect. We find that IPO-BT is not fully represented in any individual EOF of Z500 with most EOFs having a very low spatial correlation with the IPO-BT ($r < 0.15$ in the NH), except for EOF2 and EOF3, which show some resemblance with the LMR2 IPO-BT pattern in the NH ($r \sim 0.6$; Figs. 11a,b). To examine the extent to which the free-running CCSM4 can capture dynamics representative of the IPO-BT, we use a pattern matching method (Ding et al. 2019) to determine the reconstructed pattern in CCSM4 that best matches EOF2-LMR2 from all possible linear combinations of EOF2 and EOF3. It follows the coefficients a and b varying from -1 to 1 at increments of 0.1 respectively. The optimal magnitudes of each coefficient are determined by the highest spatial correlation between EOF2-LMR2 and the linear combination of EOF2-CCSM4 and EOF3-CCSM4 (in this case, $a = 0.5$ and $b = 0.5$; $r = 0.93$). Therefore, the reconstructed PC of the newly constructed EOF is obtained by averaging the PCs of EOF2 and EOF3 in CCSM4.

The reconstructed mode that best matches EOF2-LMR2 is obtained from an equal-weight combination of EOF2 and EOF3 in CCSM4, and has a spatial correlation coefficient of 0.93 with EOF2-LMR2 (Fig. 11c). This indicates that IPO-BT dynamics are represented in CCSM4, but are blended between EOFs in the free-running configuration rather than appearing as a single mode. Correlations of surface temperatures in CCSM4 with the reconstructed PC of this mode exhibit some similarity with that in LMR2 but have a weaker signal especially near the poles and tropics (Fig. 12b). Thus, it appears that the model's intrinsic variability also favors the establishment of an IPO-BT-like structure, but weakly ties the Arctic and tropics together. It is the addition of proxy data that makes the Arctic–tropical linkage stronger in LMR2, promoting the emergence of the IPO-BT as a single leading EOF mode.

Additionally, the reconstructed mode in CCSM4 is primarily characterized by low-magnitude multidecadal oscillations with the peak periodicity around 30 to 40 years (Figs. 12d,f). In contrast, PC2-LMR2 exhibits stronger low-frequency oscillations around multidecadal to centennial time scales (Figs. 12c,f). The only possibility to explain the appearance of stronger low-frequency oscillations in PC2-LMR2 is the assimilation of long proxy records into CCSM4 model results. To illustrate this, we calculate a proxy index averaged from all available 33 raw records in the NH with effective record lengths longer than 1000 years over the past two millennia, by considering the sign of each individual record's coherence with PC2-LMR2 (Fig. 12a, Table 3). This proxy index is significantly correlated with PC2-LMR2 ($r = 0.53$) for the effective sample

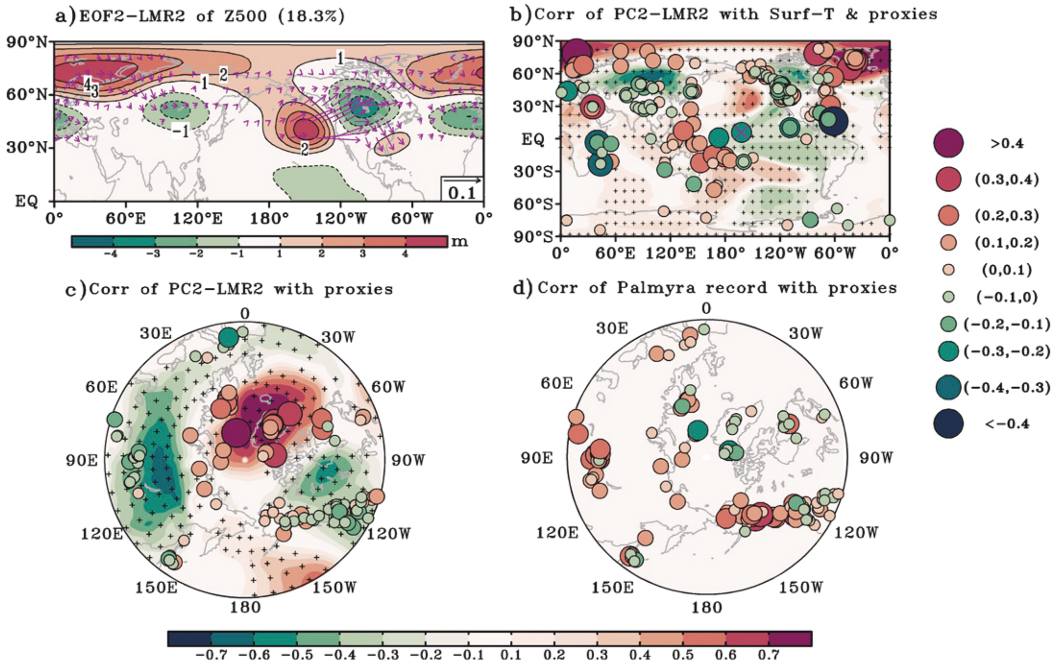

FIG. 10. (a) EOF2 of LMR2 annual mean residual Z500 (EOF2-LMR2) over the past 2000 years. (b) Correlations of PC2-LMR2 with LMR2 annual mean residual surface temperatures (shading) and proxy data (circles). (c) As in (b), but displayed in polar projection. (d) Correlations of the Palmyra coral record [5.9°N, 197.9°E; purple cross circle in (b)] with all available proxy data in the past millennium (circles) over their overlapping periods. In (a), purple vectors (10^5 Pa m^2 s^{-2}; vectors less than 10^4 Pa m^2 s^{-2} are omitted) denote the wave activity flux associated with the EOF2-LMR2. In (b) and (c), stippling indicates statistically significant correlations at the 99.9% confidence level.

size around 1000 (Fig. 12e). This confirms that it is the addition of proxy data that helps the signal of long-term variability related with the IPO-BT to emerge in the LMR2 reconstructions. Thus, this result lends us more confidence that the generation of the IPO-BT and enhancement of multidecadal variability in LMR2 is due to useful information from the real world added by proxy data on the basis of CCSM's physics, although the proxy data themselves still contain large uncertainty.

7. Conclusions and discussion

The global large-scale circulation and surface temperature patterns exhibit hemispheric asymmetric trends in the recent

TABLE 2. List of available 15 proxy records north of 70°N from the PAGES 2k version2.

Latitude (°N)	Longitude (°E)	Effective length (yr)	Archive type
80.7	286.9	1973	d180-glacier ice
80.52	94.82	1099	d180-glacier ice
79.83	24.02	554	d180-glacier ice
71.12	322.68	1421	d180-glacier ice
72.1	321.92	1170	d180-glacier ice
72.58	322.36	1979	d180-glacier ice
78.86	17.43	1229	d180-glacier ice
75.1	317.68	1996	d180-glacier ice
73.94	322.37	515	d180-glacier ice
78.4	279.6	1845	d180-glacier ice
80.78	65.63	771	d180-glacier ice
81.35	290.47	1981	sed accumulation-lake sediment
82.83	282.1	1988	varve accumulation-lake sediment
72	101	1999	trsgi-tree
70.67	125.87	505	tree

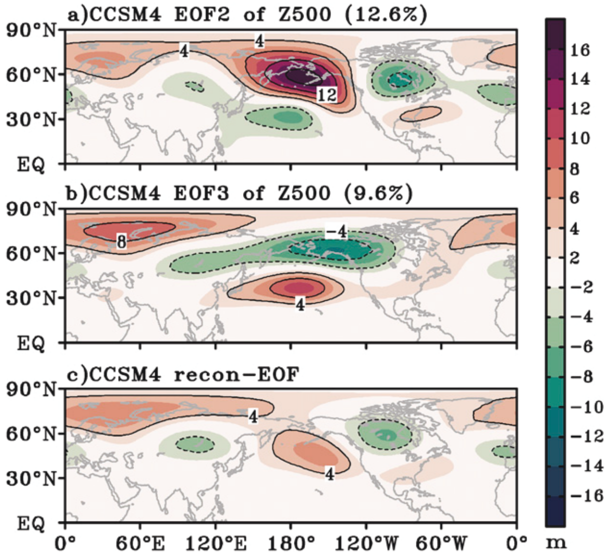

FIG. 11. (a) EOF2 and (b) EOF3 of annual mean residual Z500 in CCSM4. (c) The reconstructed mode of an equal-weight combination of EOF2-CCSM4 and EOF3-CCSM4. In (a) and (b), the total variance explained by each EOF is indicated in the parentheses.

40 years, partially driven by internal variability originating from the tropics. This tropically driven global teleconnection is referred to as the IPO-BT, emanating from the tropical eastern Pacific and propagating toward high latitudes, shaping opposite changes in the two poles and a zonal wavenumber-3 structure in the NH midlatitudes. In its positive phase, this mode is associated with a warming Arctic, cooling around most of the Antarctic and cooling tropical SST in the eastern Pacific. In addition, the WACE pattern observed in the recent 40 years may also be partially driven by this IPO-BT-related internal variability, associated with the wave train propagating along the NH subpolar waveguide, although this cooling signal over Eurasia is strongest in boreal winter. Previous studies focus on WACE's variability in the past decades, suggesting that Eurasian cooling is closely linked with sea ice loss in the Barents–Kara Seas and decadal variability in extratropical atmospheric circulation (e.g., Mori et al. 2014; Ogawa et al. 2018), while another strand of evidence indicates that the Arctic–Eurasia climate linkage could be driven by an atmospheric teleconnection originating in the tropics (e.g., Matsumura and Kosaka 2019). Here, we provide new evidence that the cooling signal over Eurasia may be associated with tropical forcing in the eastern Pacific via a Rossby wave train propagating toward the poles on low-frequency time scales in the past 400 and 2000 years, although the underlying mechanism linking the WACE with the IPO-BT remains an open question.

Furthermore, we find a consistent and prominent role of the IPO-BT in shaping global temperature variability over the past 400 and 2000 years using EKF400 and LMR2, despite uncertainty in reconstruction reanalysis resulting from inherent limitations of model simulations as well as sparse proxy data in early periods and regions such as the tropics and SH in LMR2. A strong similarity of this mode with the observed circulation trend in the past 40 years suggests that low-frequency SST variability in the tropical Pacific acts as an important internal dynamical source to jointly regulate recent polar and midlatitude climate variability along with anthropogenic forcing. This finding is partially supported by model experiments conducted by Meehl et al. (2018) suggesting that an IPO-BT-like teleconnection mode is partially driven by tropical Pacific SST forcing in winter and tropical Atlantic SST variability in summer. Due to a limitation of LMR2 in detecting seasonal differences of the IPO-BT, future work on the seasonality of the IPO-BT is needed to investigate the role of tropical SST forcing on modulating extratropical circulation changes in each season.

Low-frequency tropical Pacific SST variability serves as a prominent source of uncertainty in projections of extratropical climate variability (Coats et al. 2015; Dong and Dai 2015; Parsons et al. 2017; Cao et al. 2019). Many studies have suggested that the Atlantic meridional overturning circulation (AMOC) is one leading mode driving multidecadal variability in the NH high latitudes (Zhang et al. 2019). However, the Atlantic SST pattern associated with the IPO-BT in our study does not closely resemble AMOC (Fig. 10b). The correlation of PC2-LMR2 with a reconstructed AMOC index (Rahmstorf et al. 2015) from 900 to 1995 is 0.14, and not improved using lags from ±2 through ±50 years, suggesting that the AMOC may not directly play a role in driving the IPO-BT. Further research is needed to investigate cross-basin mechanisms of the tropical eastern Pacific and the Atlantic (Latif 2001; Cai et al. 2019) to better understand whether the AMOC could indirectly drive the IPO-BT through interactions with Pacific SST.

It is also noted that the IPO-BT is characterized by strong multidecadal and centennial variability over the past 2000 years (Figs. 12c,f), associated with low-frequency tropical SST fluctuations. Several modeling analyses have suggested that the tropical Pacific could be one birthplace of such low-frequency variability in the climate system due to basinwide atmosphere–ocean interactions associated with ocean heat content changes (Karnauskas et al. 2012), momentum flux (Larson et al. 2018) and nonlinear oceanic dynamics (Sun et al. 2014; Lewis and Legrande 2015) in the tropics and extratropics. Further accumulation and assimilation of proxy data is thus required to improve understanding of the IPO-BT's oceanic drivers and its dominant periodicity, and its global impacts and interactions with other modes of natural variability, on multidecadal and centennial time scales over the past millennia. This is particularly prevalent in the SH middle and high latitudes, where more proxy data are needed to understand whether impacts of the IPO-BT around Antarctica are stable on longer time scales. There is a growing movement in the paleoclimate community toward this goal, with more proxy data being assimilated into model simulations. This is vital to furthering our understanding of the climate system on longer time scales, since the assimilation of proxy data into the last two millennia simulations of the CCSM4-based LMR2 is integral to the enhanced representation of an important global mode of internal variability—the IPO-BT.

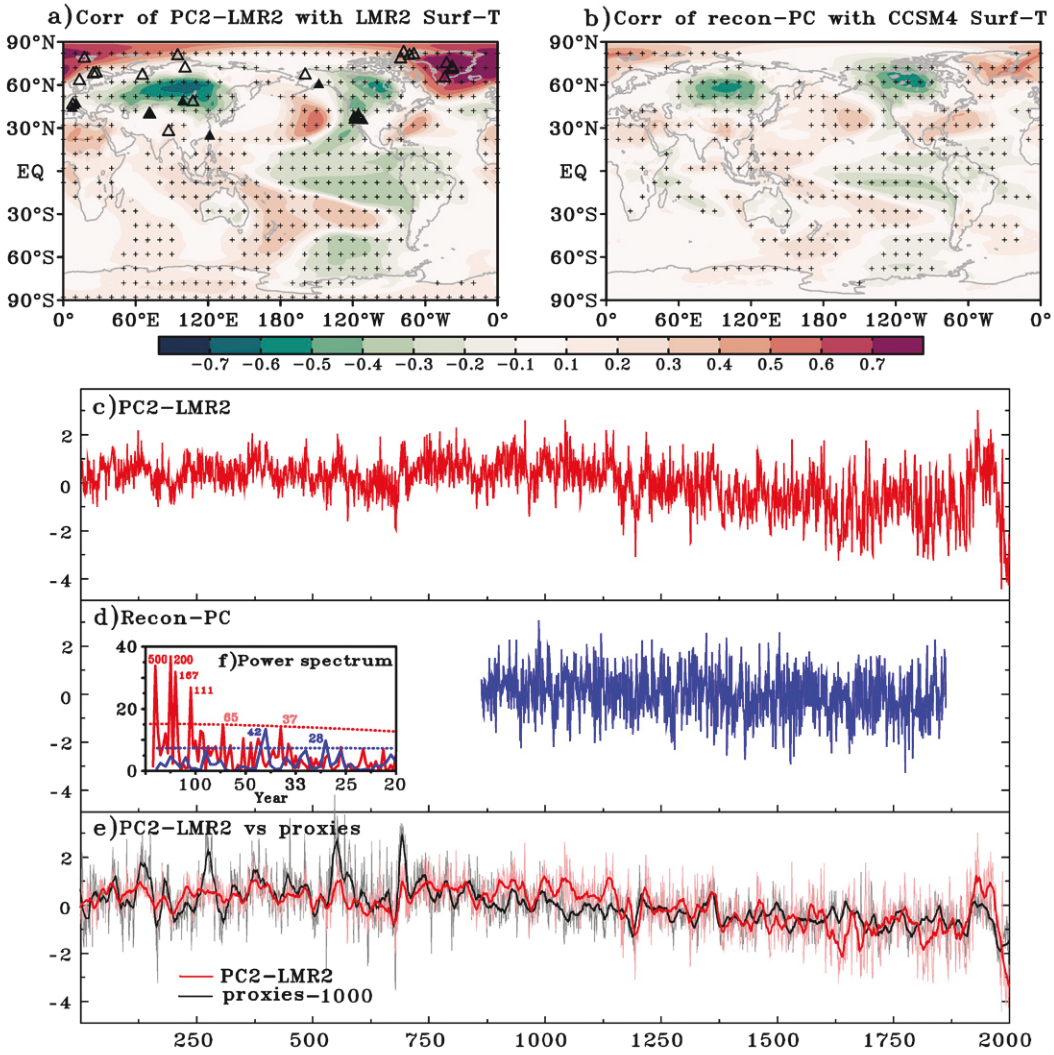

FIG. 12. (a) Correlations of PC2-LMR2 with LMR2 annual mean residual surface temperatures (shading) and proxy records owing effective record lengths longer than 1000 years. (b) Correlations of reconstructed PC with CCSM4 annual mean residual surface temperatures. Time series of (c) PC2-LMR2, (d) reconstructed PC in CCSM4, and (e) the normalized proxy index averaged from 33 proxy records, denoted as triangles in (a), considering the sign of each individual record's correlation with PC2-LMR2 (black thin curve) and a 30-yr smoothing (black bold lines). (f) The power spectra of PC2-LMR2 (red lines) and the reconstructed PC in CCSM4 (blue lines) with respective significant peaks of the spectrum highlighted (in years). In (a), hollow triangles indicate that proxy records over these sites are positively added into the total index [black thin curve in (e)] and solid triangles indicate those records added into the total index [black thin curve in (e)] with theirs signs reversed. Stippling in (a) and (b) indicates statistically significant correlations at the 99.9% confidence level with the effect sample size at 700. In (f), we calculate the theoretical Markov spectrum with dotted curves showing the 95% confidence level using the lag-1 autocorrelation.

Last, we want to emphasize that current climate models may still have some limitations in replicating some features of the observed IPO-BT, especially the linkage between the tropics and Arctic (Ding et al. 2019, Blanchard-Wrigglesworth and Ding 2019, Topál et al. 2020). The observed IPO-BT reveals an out-of-phase relationship between tropical and Arctic surface temperature variability, while most models feature a same-phase relationship in the tropics and Arctic (Screen and Deser 2019), which calls for caution in the interpretation of model simulations in the high latitudes. More future analyses are needed to pinpoint the cause of this discrepancy and understand why the tropical–Arctic linkage behaves differently between the observations and the model world.

Acknowledgments. This study was supported by Climate Variability and Predictability (NA18OAR4310424) and Modeling, Analysis, Predictions and Projections (NA19OAR4310281) programs as part of NOAA's Climate Program Office and NSF's Polar Programs (OPP-1744598, OPP-1443144). X. F. was jointly supported

TABLE 3. List of available 33 proxy records in the NH with effective record lengths longer than 1000 years presented as triangles in Fig. 12a. We construct a proxy index averaged from these 33 proxy records, considering the sign of each individual record's correlation with PC2-LMR2 (the rightmost column). The records with positive sign are positively added into the total index and vice versa.

Latitude (°N)	Longitude (°E)	Effective length (yr)	Archive type	Correlation with PC2-LMR2
80.7	286.9	1973	d180-glacier ice	Positive
80.52	94.82	1099	d180-glacier ice	Positive
71.12	322.68	1421	d180-glacier ice	Positive
65.18	316.17	1978	d180-glacier ice	Positive
72.1	321.92	1170	d180-glacier ice	Positive
72.58	322.36	1979	d180-glacier ice	Positive
78.86	17.43	1229	d180-glacier ice	Positive
75.1	317.68	1996	d180-glacier ice	Positive
78.4	279.6	1845	d180-glacier ice	Positive
81.35	290.47	1981	sed accumulation-lake sediment	Positive
82.83	282.1	1988	varve thickness-lake sediment	Positive
72	101	1999	trsgi-tree	Positive
24.53	121.38	1094	trsgi-tree	Negative
48.35	107.47	1005	trsgi-tree	Positive
27.78	87.27	1141	trsgi-tree	Positive
39.83	71.5	1126	trsgi-tree	Positive
48.3	98.93	1954	trsgi-tree	Negative
39.83	71.5	1302	trsgi-tree	Negative
47	10.7	2000	trsgi-tree	Negative
44	7.5	1032	trsgi-tree	Negative
67.1	200.4	1015	trsgi-tree	Positive
60.5	211.7	1119	trsgi-tree	Negative
36.3	241.8	1071	trsgi-tree	Positive
37.8	240.8	1197	trsgi-tree	Negative
36.4	241.8	1993	trsgi-tree	Negative
37	243.5	2000	trsgi-tree	Negative
40.2	244.5	1666	trsgi-tree	Negative
35.3	248.6	2000	trsgi-tree	Negative
68.49	27.33	1201	MXD-tree	Positive
66.9	65.6	1110	tree	Positive
63.25	13.34	1218	MXD-tree	Positive
46.4	7.8	1246	MXD-tree	Positive
68	25	2000	MXD-tree	Positive

by the China Scholarship Council (CSC) (201808320280) and NA18OAR4310424 and the National Natural Science Foundation of China (41730961). L. W. was supported by the National Natural Science Foundation of China (41730961). We acknowledge the CESM Large Ensemble Community Project, U.S. CLIVAR Large Ensemble Working Group and supercomputing resources provided by NSF/CISL/Yellowstone.

REFERENCES

Anderson, D. M., R. Tardif, K. Horlick, M. P. Erb, G. J. Hakim, D. Noone, W. A. Perkins, and E. Steig, 2019: Additions to the last millennium reanalysis multi-proxy database. *Data Sci. J.*, **18**, 2, https://doi.org/10.5334/dsj-2019-002.

Armour, K. C., J. Marshall, J. R. Scott, A. Donohoe, and E. R. Newsom, 2016: Southern Ocean warming delayed by circumpolar upwelling and equatorward transport. *Nat. Geosci.*, **9**, 549–554, https://doi.org/10.1038/ngeo2731.

Blanchard-Wrigglesworth, E., and Q. Ding, 2019: Tropical and midlatitude impact on seasonal polar predictability in the Community Earth System Model. *J. Climate*, **32**, 5997–6014, https://doi.org/10.1175/JCLI-D-19-0088.1.

Bretherton, C. S., M. Widmann, V. P. Dymnikov, J. M. Wallace, and I. Bladé, 1999: The effective number of spatial degrees of freedom of a time-varying field. *J. Climate*, **12**, 1990–2009, https://doi.org/10.1175/1520-0442(1999)012<1990:TENOSD>2.0.CO;2.

Buckley, B. M., C. C. Ummenhofer, R. D. D'Arrigo, K. G. Hansen, L. H. Truong, C. N. Le, and D. K. Stahle, 2019: Interdecadal Pacific Oscillation reconstructed from trans-Pacific tree rings: 1350–2004 CE. *Climate Dyn.*, **53**, 3181–3196, https://doi.org/10.1007/s00382-019-04694-4.

Cai, W., and Coauthors, 2019: Pantropical climate interactions. *Science*, **363**, eaav4236, https://doi.org/10.1126/science.aav4236.

Cao, D., Q. Wu, A. Hu, Y. Yao, S. Liu, S. R. Schroeder, and F. Yang, 2019: Linear and nonlinear winter atmospheric responses to extreme phases of low frequency Pacific sea surface temperature variability. *Climate Dyn.*, **52**, 49–68, https://doi.org/10.1007/s00382-018-4127-1.

Christidis, N., and P. A. Stott, 2015: Changes in the geopotential height at 500 hPa under the influence of external climatic forcings. *Geophys. Res. Lett.*, **42**, 10 798–10 806, https://doi.org/10.1002/2015GL066669.

Coats, S., J. E. Smerdon, B. I. Cook, and R. Seager, 2015: Are simulated megadroughts in the North American Southwest forced? *J. Climate*, **28**, 124–142, https://doi.org/10.1175/JCLI-D-14-00071.1.

Cobb, K. M., N. Westphal, H. R. Sayani, J. T. Watson, E. Di Lorenzo, H. Cheng, R. L. Edwards, and C. D. Charles, 2013: Highly variable El Niño–Southern Oscillation throughout the Holocene. *Science*, **339**, 67–70, https://doi.org/10.1126/science.1228246.

Cohen, J. L., J. C. Furtado, M. A. Barlow, V. A. Alexeev, and J. E. Cherry, 2012: Arctic warming, increasing snow cover and widespread boreal winter cooling. *Environ. Res. Lett.*, **7**, 014007, https://doi.org/10.1088/1748-9326/7/1/014007.

Compo, G. P., and Coauthors, 2011: The Twentieth Century Reanalysis Project. *Quart. J. Roy. Meteor. Soc.*, **137**, 1–28, https://doi.org/10.1002/qj.776.

Dee, D. P., and Coauthors, 2011: The ERA-Interim reanalysis: Configuration and performance of the data assimilation system. *Quart. J. Roy. Meteor. Soc.*, **137**, 553–597, https://doi.org/10.1002/qj.828.

Deser, C., R. Guo, and F. Lehner, 2017: The relative contributions of tropical Pacific sea surface temperatures and atmospheric internal variability to the recent global warming hiatus. *Geophys. Res. Lett.*, **44**, 7945–7954, https://doi.org/10.1002/2017GL074273.

——, and Coauthors, 2020: Insights from Earth system model initial-condition large ensembles and future prospects. *Nat. Climate Change*, **10**, 277–286, https://doi.org/10.1038/s41558-020-0731-2.

Ding, Q., E. J. Steig, D. S. Battisti, and M. Küttel, 2011: Winter warming in West Antarctica caused by central tropical Pacific warming. *Nat. Geosci.*, **4**, 398–403, https://doi.org/10.1038/ngeo1129.

——, J. M. Wallace, D. S. Battisti, E. J. Steig, A. J. E. Gallant, H. J. Kim, and L. Geng, 2014: Tropical forcing of the recent rapid Arctic warming in northeastern Canada and Greenland. *Nature*, **509**, 209–212, https://doi.org/10.1038/nature13260.

——, and Coauthors, 2019: Fingerprints of internal drivers of Arctic sea ice loss in observations and model simulations. *Nat. Geosci.*, **12**, 28–33, https://doi.org/10.1038/s41561-018-0256-8.

Dong, B., and A. Dai, 2015: The influence of the interdecadal Pacific oscillation on temperature and precipitation over the globe. *Climate Dyn.*, **45**, 2667–2681, https://doi.org/10.1007/s00382-015-2500-x.

Franke, J., S. Brönnimann, J. Bhend, and Y. Brugnara, 2017: A monthly global paleo-reanalysis of the atmosphere from 1600 to 2005 for studying past climatic variations. *Sci. Data*, **4**, 170076, https://doi.org/10.1038/sdata.2017.76.

Fu, Q., S. Manabe, and C. M. Johanson, 2011: On the warming in the tropical upper troposphere: Models versus observations. *Geophys. Res. Lett.*, **38**, L15704, https://doi.org/10.1029/2011GL048101.

Goosse, H., W. Lefebvre, A. de Montety, E. Crespin, and A. H. Orsi, 2009: Consistent past half-century trends in the atmosphere, the sea ice and the ocean at high southern latitudes. *Climate Dyn.*, **33**, 999–1016, https://doi.org/10.1007/s00382-008-0500-9.

Griffies, S. M., and Coauthors, 2011: The GFDL CM3 coupled climate model: Characteristics of the ocean and sea ice simulations. *J. Climate*, **24**, 3520–3544, https://doi.org/10.1175/2011JCLI3964.1.

Hahn, L., C. C. Ummenhofer, and Y. O. Kwon, 2018: North Atlantic natural variability modulates emergence of widespread Greenland melt in a warming climate. *Geophys. Res. Lett.*, **45**, 9171–9178, https://doi.org/10.1029/2018GL079682.

Hansen, J., R. Ruedy, M. Sato, and K. Lo, 2010: Global surface temperature change. *Rev. Geophys.*, **48**, RG4004, https://doi.org/10.1029/2010RG000345.

Henley, B. J., J. Gergis, D. J. Karoly, S. Power, J. Kennedy, and C. K. Folland, 2015: A tripole index for the interdecadal Pacific oscillation. *Climate Dyn.*, **45**, 3077–3090, https://doi.org/10.1007/s00382-015-2525-1.

Holland, P. R., and R. Kwok, 2012: Wind-driven trends in Antarctic sea-ice drift. *Nat. Geosci.*, **5**, 872–875, https://doi.org/10.1038/ngeo1627.

Huang, B., and Coauthors, 2017: Extended reconstructed sea surface temperature, version 5 (ERSSTv5): Upgrades, validations, and intercomparisons. *J. Climate*, **30**, 8179–8205, https://doi.org/10.1175/JCLI-D-16-0836.1.

Ji, F., Z. Wu, J. Huang, and E. P. Chassignet, 2014: Evolution of land surface air temperature trend. *Nat. Climate Change*, **4**, 462–466, https://doi.org/10.1038/nclimate2223.

Kalnay, E., and Coauthors, 1996: The NCEP/NCAR 40-Year Reanalysis Project. *Bull. Amer. Meteor. Soc.*, **77**, 437–471, https://doi.org/10.1175/1520-0477(1996)077<0437:TNYRP>2.0.CO;2.

Karnauskas, K. B., J. E. Smerdon, R. Seager, and J. F. González-Rouco, 2012: A Pacific centennial oscillation predicted by coupled GCMs. *J. Climate*, **25**, 5943–5961, https://doi.org/10.1175/JCLI-D-11-00421.1.

Kay, J. E., and Coauthors, 2015: The Community Earth System Model (CESM) large ensemble project: A community resource for studying climate change in the presence of internal climate variability. *Bull. Amer. Meteor. Soc.*, **96**, 1333–1349, https://doi.org/10.1175/BAMS-D-13-00255.1.

Kirchmeier-Young, M. C., F. W. Zwiers, and N. P. Gillett, 2017: Attribution of extreme events in Arctic sea ice extent. *J. Climate*, **30**, 553–571, https://doi.org/10.1175/JCLI-D-16-0412.1.

Kobayashi, S., and Coauthors, 2015: The JRA-55 reanalysis: General specifications and basic characteristics*J. Meteor. Soc. Japan*, **93**, 5–48, https://doi.org/10.2151/jmsj.2015-001.

Lacis, A. A., G. A. Schmidt, D. Rind, and R. A. Ruedy, 2010: Atmospheric CO_2: Principal control knob governing Earth's temperature. *Science*, **330**, 356–359, https://doi.org/10.1126/science.1190653.

Landrum, L., B. L. Otto-Bliesner, E. R. Wahl, A. Conley, P. J. Lawrence, N. Rosenbloom, and H. Teng, 2013: Last millennium climate and its variability in CCSM4. *J. Climate*, **26**, 1085–1111, https://doi.org/10.1175/JCLI-D-11-00326.1.

Larson, S. M., D. J. Vimont, A. C. Clement, and B. P. Kirtman, 2018: How momentum coupling affects SST variance and large-scale Pacific climate variability in CESM. *J. Climate*, **31**, 2927–2944, https://doi.org/10.1175/JCLI-D-17-0645.1.

Latif, M., 2001: Tropical Pacific/Atlantic Ocean interactions at multi-decadal time scales. *Geophys. Res. Lett.*, **28**, 539–542, https://doi.org/10.1029/2000GL011837.

Lewis, S. C., and A. N. Legrande, 2015: Stability of ENSO and its tropical Pacific teleconnections over the Last Millennium. *Climate Past*, **11**, 1347–1360, https://doi.org/10.5194/cp-11-1347-2015.

Maher, N., and Coauthors, 2019: The Max Planck Institute Grand Ensemble: Enabling the exploration of climate system variability. *J. Adv. Model. Earth Syst.*, **11**, 2050–2069, https://doi.org/10.1029/2019MS001639.

Maksym, T., S. E. Stammerjohn, S. Ackley, and R. Massom, 2012: Antarctic sea ice—A polar opposite? *Oceanography*, **25**, 140–151, https://doi.org/10.5670/oceanog.2012.88.

Marshall, J., K. C. Armour, J. R. Scott, Y. Kostov, U. Hausmann, D. Ferreira, T. G. Shepherd, and C. M. Bitz, 2014: The ocean's role in polar climate change: Asymmetric Arctic and Antarctic responses to greenhouse gas and ozone forcing. *Philos. Trans. Roy. Soc.*, **372A**, 20130040, https://doi.org/10.1098/rsta.2013.0040.

——, J. R. Scott, K. C. Armour, J. M. Campin, M. Kelley, and A. Romanou, 2015: The ocean's role in the transient response of climate to abrupt greenhouse gas forcing. *Climate Dyn.*, **44**, 2287–2299, https://doi.org/10.1007/s00382-014-2308-0.

Matsumura, S., and Y. Kosaka, 2019: Arctic–Eurasian climate linkage induced by tropical ocean variability. *Nat. Commun.*, **10**, 3441, https://doi.org/10.1038/s41467-019-11359-7.

Meehl, G. A., C. T. Y. Chung, J. M. Arblaster, M. M. Holland, and C. M. Bitz, 2018: Tropical decadal variability and the rate of Arctic sea ice decrease. *Geophys. Res. Lett.*, **45**, 11 326–11 333, https://doi.org/10.1029/2018GL079989.

Mori, M., M. Watanabe, H. Shiogama, J. Inoue, and M. Kimoto, 2014: Robust Arctic sea-ice influence on the frequent Eurasian cold winters in past decades. *Nat. Geosci.*, **7**, 869–873, https://doi.org/10.1038/ngeo2277.

Ogawa, F., and Coauthors, 2018: Evaluating impacts of recent Arctic sea ice loss on the Northern Hemisphere winter climate change. *Geophys. Res. Lett.*, **45**, 3255–3263, https://doi.org/10.1002/2017GL076502.

Overland, J., J. A. Francis, R. Hall, E. Hanna, S. Kim, and T. Vihma, 2015: The melting Arctic and midlatitude weather patterns: Are they connected? *J. Climate*, **28**, 7917–7932, https://doi.org/10.1175/JCLI-D-14-00822.1.

PAGES2k Consortium, 2017: A global multiproxy database for temperature reconstructions of the Common Era. *Sci. Data*, **4**, 170088, https://doi.org/10.1038/sdata.2017.88.

Parsons, L. A., G. R. Loope, J. T. Overpeck, T. R. Ault, R. Stouffer, and J. E. Cole, 2017: Temperature and precipitation variance in CMIP5 simulations and paleoclimate records of the last millennium. *J. Climate*, **30**, 8885–8912, https://doi.org/10.1175/JCLI-D-16-0863.1.

Phipps, S. J., L. D. Rotstayn, H. B. Gordon, J. L. Roberts, A. C. Hirst, and W. F. Budd, 2011: The CSIRO Mk3L climate system model version 1.0—Part 1: Description and evaluation. *Geosci. Model Dev.*, **4**, 483–509, https://doi.org/10.5194/gmd-4-483-2011.

——, ——, ——, ——, ——, and ——, 2012: The CSIRO Mk3L climate system model version 1.0—Part 2: Response to external forcings. *Geosci. Model Dev.*, **5**, 649–682, https://doi.org/10.5194/gmd-5-649-2012.

Plumb, R. A., 1985: On the three-dimensional propagation of stationary waves. *J. Atmos. Sci.*, **42**, 217–229, https://doi.org/10.1175/1520-0469(1985)042<0217:OTTDPO>2.0.CO;2.

Polyakov, I. V., and Coauthors, 2017: Greater role for Atlantic inflows on sea-ice loss in the Eurasian Basin of the Arctic Ocean. *Science*, **356**, 285–291, https://doi.org/10.1126/science.aai8204.

——, T. P. Rippeth, I. Fer, M. B. Alkire, T. M. Baumann, E. C. Carmack, and L. Padman, 2020: Weakening of cold halocline layer exposes sea ice to oceanic heat in the eastern Arctic Ocean. *J. Climate*, **33**, 8107–8123, https://doi.org/10.1175/JCLI-D-19-0976.1.

Rahmstorf, S., J. E. Box, G. Feulner, M. E. Mann, A. Robinson, S. Rutherford, and E. J. Schaffernicht, 2015: Exceptional twentieth-century slowdown in Atlantic Ocean overturning circulation. *Nat. Climate Change*, **5**, 475–480, https://doi.org/10.1038/nclimate2554.

Schneider, D. P., and E. J. Steig, 2008: Ice cores record significant 1940s Antarctic warmth related to tropical climate variability. *Proc. Natl. Acad. Sci. USA*, **105**, 12 154–12 158, https://doi.org/10.1073/pnas.0803627105.

Screen, J. A., and I. Simmonds, 2010: The central role of diminishing sea ice in recent Arctic temperature amplification. *Nature*, **464**, 1334–1337, https://doi.org/10.1038/nature09051.

——, and C. Deser, 2019: Pacific Ocean variability influences the time of emergence of a seasonally ice-free Arctic Ocean. *Geophys. Res. Lett.*, **46**, 2222–2231, https://doi.org/10.1029/2018GL081393.

Serreze, M. C., and R. G. Barry, 2011: Processes and impacts of Arctic amplification: A research synthesis. *Global Planet. Change*, **77**, 85–96, https://doi.org/10.1016/j.gloplacha.2011.03.004.

——, A. P. Barrett, J. C. Stroeve, D. N. Kindig, and M. M. Holland, 2009: The emergence of surface-based Arctic amplification. *Cryosphere*, **3**, 11–19, https://doi.org/10.5194/tc-3-11-2009.

Stickler, A., and Coauthors, 2014: ERA-CLIM: Historical surface and upper-air data for future reanalyses. *Bull. Amer. Meteor. Soc.*, **95**, 1419–1430, https://doi.org/10.1175/BAMS-D-13-00147.1.

Sun, D. Z., T. Zhang, Y. Sun, and Y. Yu, 2014: Rectification of El Niño–Southern Oscillation into climate anomalies of decadal and longer time scales: Results from forced ocean GCM experiments. *J. Climate*, **27**, 2545–2561, https://doi.org/10.1175/JCLI-D-13-00390.1.

Sun, L., J. Perlwitz, and M. Hoerling, 2016: What caused the recent ''warm Arctic, cold continents'' trend pattern in winter temperatures? *Geophys. Res. Lett.*, **43**, 5345–5352, https://doi.org/10.1002/2016GL069024.

Tardif, R., and Coauthors, 2019: Last Millennium Reanalysis with an expanded proxy database and seasonal proxy modeling. *Climate Past*, **15**, 1251–1273, https://doi.org/10.5194/cp-15-1251-2019.

Taylor, K. E., R. J. Stouffer, and G. A. Meehl, 2012: An overview of CMIP5 and the experiment design. *Bull. Amer. Meteor. Soc.*, **93**, 485–498, https://doi.org/10.1175/BAMS-D-11-00094.1.

Topál, D., Q. Ding, J. Mitchell, I. Baxter, M. Herein, T. Haszpra, R. Luo, and Q. Li, 2020: An internal atmospheric process determining summertime Arctic sea ice melting in the next three decades: Lessons learned from five large ensembles and multiple CMIP5 climate simulations. *J. Climate*, **33**, 7431–7454, https://doi.org/10.1175/JCLI-D-19-0803.1.

Trenberth, K. E., J. T. Fasullo, G. Branstator, and A. S. Phillips, 2014: Seasonal aspects of the recent pause in surface warming. *Nat. Climate Change*, **4**, 911–916, https://doi.org/10.1038/nclimate2341.

Uppala, S. M., and Coauthors, 2005: The ERA-40 Re-Analysis. *Quart. J. Roy. Meteor. Soc.*, **131**, 2961–3012, https://doi.org/10.1256/qj.04.176.

Vaughan, D. G., and Coauthors, 2013: Observations: Cryosphere. *Climate Change 2013: The Physical Science Basis*, T. F. Stocker et al., Eds., Cambridge University Press, 317–382.

Vinther, B. M., and Coauthors, 2008: Synchronizing ice cores from the Renland and Agassiz ice caps to the Greenland Ice Core Chronology. *J. Geophys. Res.*, **113**, D08115, https://doi.org/10.1029/2007JD009143.

Zhang, R., R. Sutton, G. Danabasoglu, Y. O. Kwon, R. Marsh, S. G. Yeager, D. E. Amrhein, and C. M. Little, 2019: A review of the role of the Atlantic meridional overturning circulation in Atlantic multidecadal variability and associated climate impacts. *Rev. Geophys.*, **57**, 316–375, https://doi.org/10.1029/2019RG000644.